Topology of the Electron Density and Cohesive Energy of the Face-Centered Cubic Transition Metals

Yosslen Aray,* Jesus Rodriguez, and David Vega†

Centro de Quimica, IVIC, Apartado 21827, Caracas 1020 A, Venezuela

Received: November 9, 1999; In Final Form: February 21, 2000

The topology of the electron density for face-centered cubic transition metals (β-Co, Ni, Cu, Rh, Pd, Ag, Ir, Pt, and Au) was studied. All of the electron density critical points in the unit cell were systematically calculated. The network of bond paths describing the atomic connectivity confirms that the crystal graph of these metals is the result of packing octahedra and tetrahedra. A good correlation between the experimental cohesive energy and the value of the electronic charge density at the bond critical point corroborates that this latter parameter provides a measure of the bond strength in the case of the transition metals studied.

1. Introduction

The topological theory of Bader et al. provides a rigorous definition of chemical bonds in all classes of molecules and solids.[1−4] This theory makes use of the total electron density, $\rho(\mathbf{r})$, of a molecule or solid to determine its topology. This topology is characterized by its critical points (CPs): maxima, minima, and saddles points. In general, $\rho(\mathbf{r})$ exhibits local maxima only at the nuclear positions and a saddle point between each pair of bonded nuclei. The latter is called a *bond critical point*, and its presence is a necessary condition for the existence of a chemical bond.[1,2] A unique pair of trajectories of the vector field $\nabla\rho(\mathbf{r})$, which originate at the bond critical point, define a line linking the nuclei, on which the electron density is a maximum with respect to any other neighboring line. This is a *bond path*, and its presence is a necessary and sufficient condition for the existence of a bond.[2] A bond path determines and characterizes all of the atomic interactions in a given system. Bader's theory has been extensively applied to a number of organic molecules[1] but not many studies have been devoted to solid-state systems.[5−16] The connection between the topology of the electron density and the chemical and structural stability of isolated molecules has been well-established.[1] In particular, it has been observed that the stability of a molecule correlates with the values of the electron density at the bond critical point, ρ_b.[1] Systematic studies of these relationships in periodic solids are scarce. To our knowledge, only two such studies have been reported.[5,14] Zou and Bader[5] found that the calculated binding energies of a set of semiconductors diamond and silicon (in the diamond structure) and SiC, BN, and AlP (in the zinc blende structure) exhibit the same trend in values as ρ_b, decreasing from a maximum in diamond to a minimum in AlP. Luaña, Costales, and Pendás[14] performed topological analyses of 120 ionic perovskites of the form AMX_3 (A = Li, Na, K, Rb, and Cs; M = Be, Mg, Ca, Sr, Ba, and Zn; X = F, Cl, Br, and I). They plotted the total binding energy against ρ_b, the density at the M−X bond CP, and found that the binding energies of those crystals having a common M are proportional to $\rho_b^{1/3}$. To verify this kind of relationship in transition metals, we have carried out, in the present study, a systematic determination of the topology of the electron density of the faced-centered cubic transition metals, fccTM, and have explored the correlation of the calculated ρ_b with the experimentally reported cohesive energy values.

2. Theory

The topological properties of a crystal charge distribution are summarized by its critical points (CP).[1] These are points at which the gradient vector field, $\nabla\rho(\mathbf{r})$ vanishes, and they are classified by the $\rho(\mathbf{r})$ curvatures or three eigenvalues λ_i (i = 1, 2, and 3) of the Hessian matrix ($H_{ij} = \partial^2\rho(\mathbf{r})/\partial x_i\,\partial x_j$). They are labeled by their rank (number of nonzero eigenvalues) and signatures (excess number of positive over negative eigenvalues) and correspond to maxima (3,−3), minima (3,+3), and saddle points ((3,+1) and (3,−1)). Every CP has a characteristic pattern of trajectories or gradient paths of $\rho(\mathbf{r})$. The trajectories originate and end at critical points. Only the (3,−3) points are three-dimensional trajectory attractors: trajectories only terminate at this CP. The (3,−3) points generally occur at the nuclear positions, so that each nucleus is a three-dimensional point attractor in the vector field $\nabla\rho(\mathbf{r})$. The region traversed by the gradient paths, which terminate at a given attractor, is called the *basin* of the attractor. A (3,−1) CP is found between every pair of neighboring nuclei. It represents both local maxima in two directions and a local minimum in the third direction and is called a bond critical point *(b)*. The gradient paths associated with the negative eigenvalues at the (3,−1) point terminate at this CP and define the zero-flux surfaces that partition the crystal into unique fragments (the *atomic basins*). The unique pair of trajectories associated with the positive eigenvalue of the (3,−1) CP originate at this point and terminate at the neighboring attractors. These two unique gradient paths define a line (the bond path) linking the nuclei (*n*), along which the charge density is a maximum with respect to any neighboring line. The network of bond paths defines a graph, the *crystal graph*, which describes the atomic connectivity and structure within a crystal cell. The other CPs occurs as a consequence of the geometrical arrangements of bond paths, and they define the remaining elements of crystal structure, rings, and cages. If the bond paths are linked to form a ring of bonded atoms, then a (3,+1) CP is found in the interior of the ring. The eigenvectors associated

* To whom correspondence should be addressed. E-mail: yaray@quimica.ivic.ve. Fax: (58) 2 504 1350.

† Permanent address: FACYT. Universidad de Carabobo, Valencia, Venezuela. E-mail: dvega@thor.uc.edu.ve.

10.1021/jp993976a CCC: $19.00
Published on Web 04/21/2000

with the two positive eigenvalues of the (3,+1) or *ring* (*r*) CP generate an infinite set of gradient paths that originate at the CP and define a surface, called the ring surface. All of these trajectories terminate at the ring nuclei or at the bond CPs, whose bond paths form the perimeter of the ring. The single negative eigenvector of the ring CP generates a pair of gradient paths, which terminate at the CP and define a unique axis perpendicular to the ring surface at the critical point. The (3,+3) or *cage* (*c*) CPs are located inside a cage nuclear arrangement. The charge density is a local minimum at a cage CP, and in crystals, it is the main source of trajectories of $\nabla\rho(\mathbf{r})$: trajectories only originate at such CPs and terminate at nuclei, bond or ring CPs. The type and numbers of CPs for an extended system[5] satisfy the Poincaré−Hopf formula

$$n - b + r - c = 0$$

3. Method

The electron densities were calculated by means of the WIEN-97[18] program using a Kohn−Sham Hamiltonian that includes the generalized gradient approximation of Perdew et al.[19] and the unrestricted scheme to obtain spin-polarized wave functions. WIEN-97 contains a full-potential linearized augmented plane-wave (FLAPW) method[18] that is considered to be among the most accurate methods for performing electronic structure calculations for crystals. The unit cell is divided into nonoverlapping atomic spheres (centered at the atomic sites) called muffin-tins, MT, and interstitial regions, IT. In the two types of regions, different basis set are utilized: a linear combination of radial functions times spherical harmonics inside the atomic sphere and a plane wave expansion in the interstitial region. In the present work, a sphere radius, R_{MT}, equal to 2.2 au was used, with the exception of silver and gold, for which a $R_{MT} =$ 2.5 au was utilized. Inside the spheres, the potential and charge density were expanded in lattice harmonics up to $l = 12$. A basis set size of about 380 augmented plane-waves per atom with cutoffs $R_{MT}K_{max} = 9.0$ was used. Fifty-six points over the Brillouin Zone and quadratic tetrahedron method were chosen for k-space numerical integration. The topology of $\rho(\mathbf{r})$ was analyzed using a local version of the EXTREM program[20] contained in the EXCUBO[21] program and adapted to WIEN 97 code.

4. Results and Discussion

4.1 Topological Structure of the Electronic Density. The lattices of fccTM[22] are described by the space group *Fm*3*m* with cube edge length $a =$ 3.5440, 3.5236, 3.6147, 3.8044, 3.8907, 4.0857, 3.8389, 3.9239, and 4.0788 Å for β-Co, Ni, Cu, Rh, Pd, Ag, Ir, Pt, and Au, respectively. In this lattice, the atomic coordination number is 12, each atom being surrounded by 12 first nearest neighbors at a distance of $a\sqrt{2}/2$ and six second nearest neighbors at a distance a. Previous studies[6−11] have found bond critical points midway between nearest neighbors, suggesting the formation of two types of polyhedra sharing their faces: octahedra and tetrahedra with a *c* CP at the center and eight and four *r* CPs at the faces, respectively. Those studies reported only the topological properties of the electron density at the *b* CPs. In the present work, we have located all of the CPs; the parameters that characterize them are given in Table 1. In Table 1, the corresponding Wyckoff letter in the International Tables of Crystallography[23] identifies the critical points within a unit cell. This identification is useful in determining the topology of the electron density of an extended system. There are 4 nuclei in the primitive cell, located at the

TABLE 1: Topological Properties (au) of $\rho(\mathbf{r})$ at the Critical Points for Bulk fcc Transition Metals

Wyckoff letter	critical point	$\mathbf{r}_c$	$\rho(\mathbf{r}_c)$	λ_1	λ_2	λ_3	$\mathbf{r}_c$	$\rho(\mathbf{r}_c)$	λ_1	λ_2	λ_3	$\mathbf{r}_c$	$\rho(\mathbf{r}_c)$	λ_1	λ_2	λ_3
		β-Co					Ni					Cu				
e 24	**bond**	2.371 82	0.048 28	−0.028 49	−0.017 57	0.109 62	2.35417	0.046 95	−0.028 18	−0.020 77	0.119 75	2.424 21	0.038 99	−0.021 99	−0.016 16	0.102 52
f 32	**ring**	2.757 57	0.040 32	−0.009 07	0.028 77	0.028 77	2.73092	0.038 59	−0.009 39	0.028 15	0.028 15	2.809 24	0.031 93	−0.008 08	0.022 82	0.022 82
b 4	**octahedral cage**	3.354 27	0.027 47	0.010 33	0.010 33	0.010 33	3.329 30	0.025 64	0.012 32	0.012 32	0.012 32	3.428 35	0.021 33	0.010 00	0.010 00	0.010 00
c 8	**tetrahedral cage**	2.904 88	0.039 56	0.013 16	0.013 16	0.013 16	2.883 26	0.037 72	0.012 47	0.012 47	0.012 47	2.969 04	0.031 07	0.010 51	0.010 51	0.010 51
		Rh					Pd					Ag				
e 24	**bond**	2.541 79	0.054 47	−0.037 09	−0.032 78	0.175 46	2.599 45	0.043 63	−0.029 12	−0.025 63	0.163 12	2.729 74	0.032 03	−0.019 16	−0.016 12	0.104 46
f 32	**ring**	2.940 68	0.040 23	−0.012 81	0.040 44	0.040 44	3.006 13	0.032 04	−0.010 36	0.030 59	0.030 59	3.156 84	0.023 11	−0.006 92	0.024 70	0.024 70
b 4	**octahedral cage**	3.594 64	0.023 80	0.013 65	0.013 65	0.013 65	3.676 18	0.018 44	0.011 94	0.011 94	0.011 94	3.860 43	0.014 00	0.006 59	0.006 59	0.006 59
c 8	**tetrahedral cage**	3.113 05	0.038 46	0.017 23	0.017 23	0.017 23	3.183 67	0.030 51	0.012 80	0.012 80	0.012 80	3.343 23	0.021 85	0.010 81	0.010 81	0.010 81
		Ir					Pt					Au				
e 24	**bond**	2.564 84	0.066 04	−0.044 38	−0.041 31	0.184 59	2.621 63	0.055 30	−0.038 01	−0.035 38	0.179 53	2.725 13	0.041 56	−0.026 84	−0.025 22	0.145 23
f 32	**ring**	2.965 04	0.048 78	−0.027 70	0.040 59	0.040 59	3.030 04	0.039 26	−0.016 30	0.039 80	0.039 80	3.148 92	0.028 80	−0.010 28	0.033 29	0.033 29
b 4	**octahedral cage**	3.627 24	0.025 46	0.022 22	0.022 22	0.022 22	3.707 55	0.020 24	0.016 85	0.016 85	0.016 85	3.853 91	0.015 14	0.010 34	0.010 34	0.010 34
c 8	**tetrahedral cage**	3.141 28	0.045 91	0.019 79	0.019 79	0.019 79	3.210 83	0.036 67	0.018 20	0.018 20	0.018 20	3.337 58	0.026 90	0.013 80	0.013 80	0.013 80

position labeled **a**, 24 bond critical points at position **e**, 32 ring critical points at **f**, 4 octahedral cage critical points at **b**, and 8 tetrahedral cage critical points at points at **c**. Additionally, the topologically defined elements of the fcc structure for the case of Ni are illustrated in Figures 1 and 2. The patterns of the trajectories of $\nabla\rho(\mathbf{r})$ in the (100) and (110) planes are displayed in Figure 1. In Figure 2, we show the 3D CP's position in the crystal. In Figure 1, each line represents a trajectory of $\nabla\rho(\mathbf{r})$. A (3,−3) CP, located at each one of the nuclear positions, serves as the end point for the paths starting at the cage CPs. The volume spanned by these paths defines the basin of the atom. There are 14 cage, 6 octahedral, and 8 tetrahedral critical points defining an atom (See Figure 2). The paths that originate at four cages and terminate at a *b* CP define an interatomic surface (Figure 1c). The pair of trajectories, which originate at the *c* points and terminate at each *r* point, forms the perimeter of the surface. There is a set of twelve such surfaces bounding the atomic basin (just the Wigner−Seitz cell). In Figure 1, heavy lines show the pair of trajectories, which originate at the *b* CPs and define the bond paths. The network of bond paths (Figure 3) describing the atomic connectivity confirms that the crystal graph of the fccTM results from the packing octahedra and tetrahedra. Additionally, the curvatures of $\rho(\mathbf{r})$ at the *b* CPs are intimately related to the nature of the chemical bond.[24−27] The electron density is a maximum in the interatomic surface at *b*. The two curvatures perpendicular to the bond path, λ_1 and λ_2, are therefore negative, and the charge is locally concentrated in the surface at this CP. The negative curvatures are connected to the perpendicular contraction of $\rho(\mathbf{r})$, which leads to a contraction or compression of charge toward *b*.[24] The electron density is a minimum at the CP along the bond path, and the curvature, which is parallel to the bond path λ_3, is positive. The charge is locally depleted at the CP with respect to neighboring points on the bond path. λ_3 is related to the parallel expansion of $\rho(\mathbf{r})$, which leads to its depletion away from *b*.[1] Thus, the formation of an interatomic surface and a chemical bond is the result of a competition between those perpendicular compression and parallel expansion of $\rho(\mathbf{r})$.[24] The sign of $\nabla^2\rho$ (the sum of the tree curvatures at each point in space) at *b* determines which of the two competing effects is dominant. For cases in which $\nabla^2\rho < 0$ and is large in magnitude, $\rho(\mathbf{r})$ is also large, and the electronic charge is concentrated in the internuclear region as a result of the dominance of the perpendicular contractions of the electron density toward the bond path. The result is a sharing of the electronic charge between the atoms, as is found in covalent or polar bonds, and they are called shared interactions.[24] For cases in which $\nabla^2\rho > 0$, one has the other limiting type of atomic interaction that is dominated by contractions of $\rho(\mathbf{r})$ toward each of the nuclei as reflected in the dominance of λ_3. They are called closed-shell interactions, as they typify interactions between closed-shell atoms, as can be found in noble gas repulsive states, ionic bonds, hydrogen bonds, and van der Waals molecules.[24] Typical ρ_b values in shared interactions are 0.722, 0.551, and 0.252 au for N_2, O_2, and CC bond in ethane molecules, respectively.[1] On the other hand, in closed interactions they are 0.046, 0.036, and 0.035 au for LiCl molecules, NaCl molecules,[1] and MgO crystals,[11] respectively. The data given in Table 1 shows that the bonds of the metals studied here present characteristics associated with closed-shell type interactions: ρ_b is small and λ_3 dominates for all of the cases. A contour map of the Laplacian distribution, shown in Figure 4, corroborates the fact that the metallic interactions are dominated by the contraction of electron density, away from the interatomic surface and toward each of the nuclei. The

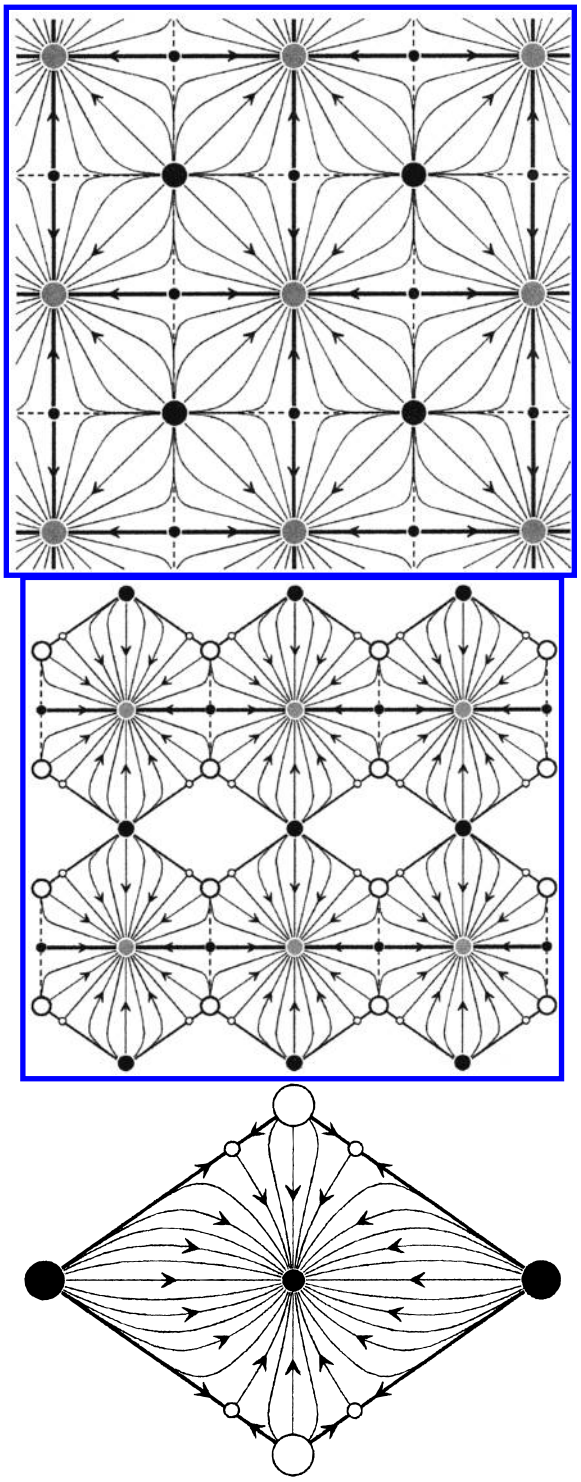

Figure 1. Trajectories traced out by gradient vectors of the electron density: trajectories of $\nabla\rho$, in (a) the (100) and (b) the (110) planes of fcc TM. The region of space traversed by trajectories, which originate at cage critical points (large black and open dots denotes octahedral and tetrahedral cages, respectively) and terminate at a given nucleus (denoted by a gray filled dot), defines the basin of the atom. Arrows show the direction of some chosen trajectories. The pair of trajectories (indicated by dotted lines) that terminates at each bond critical point (denoted by small black dots) mark the intersection of an interatomic surface with the plane of the figure. Heavy lines show the unique pair of trajectories that originate at the bond critical points and define the bond paths. The remaining critical point or ring critical points are denoted by small open dots. (c) The set of trajectories that terminates at each bond critical point defines an interatomic surface. The pairs of trajectories that originate at the ring critical points define the perimeter of the interatomic surface.

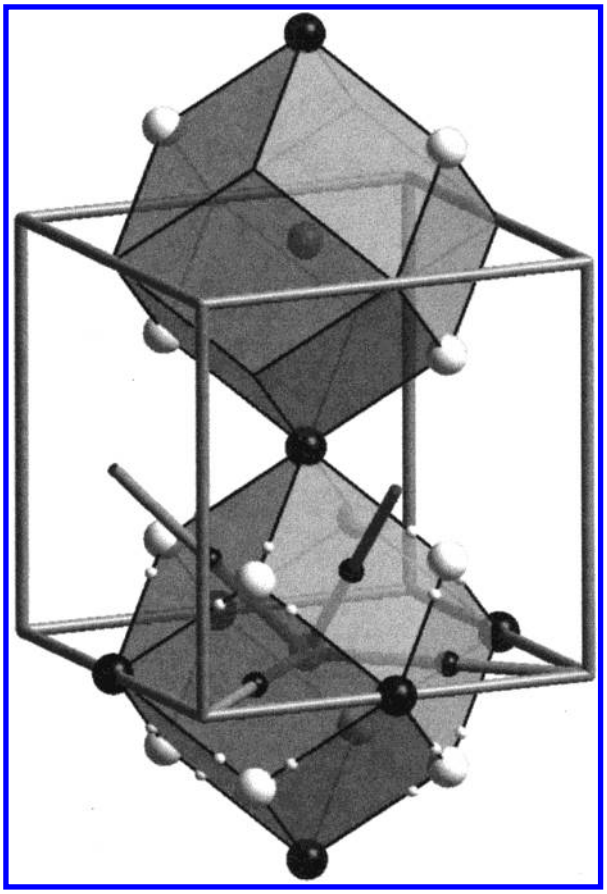

Figure 2. Basin of two neighbor atoms (gray spheres) in fcc transition metals. The cube denotes the unit cell. Large black and white spheres denote the octahedral and tetrahedral cages, whereas small black and white spheres denote the bond and ring critical points, respectively. Top basin only shows the cage critical points drawn in Figure 1b.

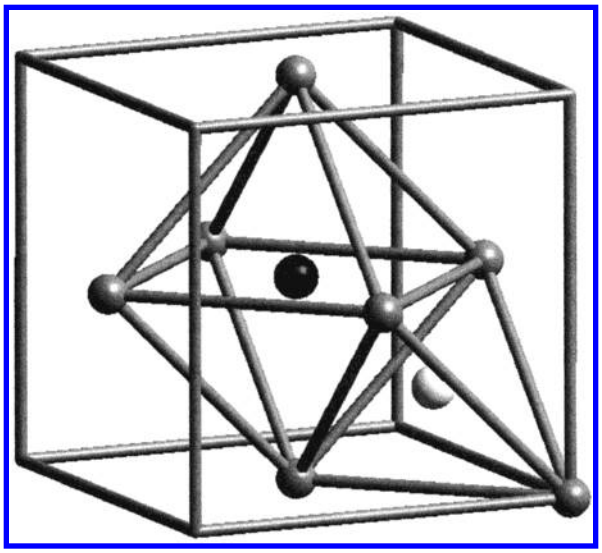

Figure 3. Crystal graph characteristic of fcc transition metals. The cube denotes the unit cell. Gray, black, and white spheres denote the nuclei, octahedral, and tetrahedral cages, respectively. Lines between each pair of atoms denote bond paths.

regions where the Laplacian is negative are identical in form to those of a free atom or ion. The Laplacian is positive over the entire region of interaction, and the kinetic energy contribution,[1] to the virial from this region, is greater than the contribution coming from the potential energy. Therefore, electrons have high mobility in the interaction zone. Thus, the topological theory

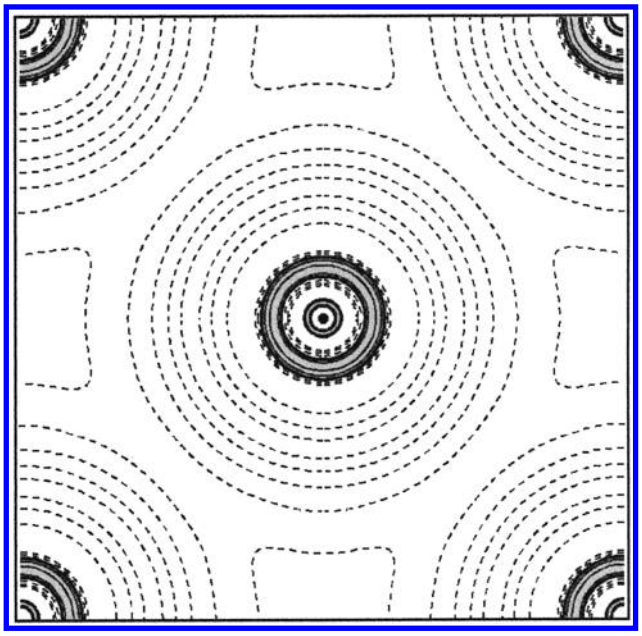

Figure 4. Contour map of $\nabla^2\rho$ on the (100) plane for the Cu bulk. Solid contours denote negative values of $\nabla^2\rho$, that is, concentration of electronic charge (shaded zones); broken contours denote regions of charge depletion.

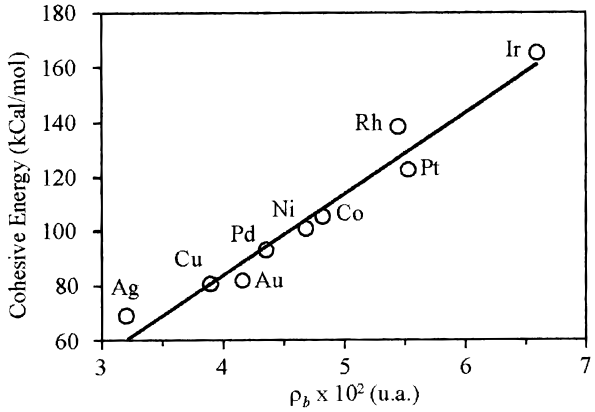

Figure 5. Experimental cohesive energy of the fcc transition metals as a function of the calculated ρ_b values.

of $\rho(\mathbf{r})$ leads us to the "gas" model for a metal. Consequently, it should be thought of as an assemblage of positive ions immersed in a small cloud of relatively "free" electrons. The electrons in this cloud are not bound to any particular ion but move rapidly through the metal. Metallic crystals are held together by the electrostatic attraction between this "gas" of negative electrons and the positively charged ions.

4.2 Cohesive Energies and the Bond Critical Points. It is well known that the value of the electron density at *b*, ρ_b, is closely related to the stability of a molecule.[1,24,27] In fact, the strength of the bonding between a given pair of atoms increases as the amount of charge in the interatomic surface for the equilibrium bond length value, as monitored by its maximum, ρ_b, increases.[1] The cohesive energy, E_{cohe}, of a crystal is defined as the energy necessary to dissociate the solid into separated atoms, molecules, or ions, as appropriate.[28] E_{cohe} is just the chemical binding force keeping the atoms together. Therefore, as in the case of molecules, we also expect that there should exist in crystals a relationship between ρ_b of the different bond CPs and E_{cohe}. To compare the bond strength of a given bond with its ρ_b for a crystal containing several types of bonds, an appropriate partition of the total cohesive energy must be

applied. For crystals with just one type of bond, E_{cohe} divided by the number of bonds per Wigner−Seitz cell gives the bond strength. In the series of crystals with only one kind of bond and with the same atomic structure, the total E_{cohe} gives the right trend for the bond strength. This is the case for the fccTM, for which the cohesive energy results from the interaction of each one of the atoms with its 12 first-nearest neighbors, as indicated by 12 bond paths. In Figure 5, we have plotted the experimental reported E_{cohe} values[28,29] versus the ρ_b from Table 1. Not surprisingly, we found a pattern that shows that ρ_b in fccTM is essentially proportional to E_{cohe}. ρ_b systematically decreases from Ir, with the strongest atomic binding, to Ag, with the weakest binding. This result verifies that ρ_b also provides a measure of the bond strength in the transition metals studied in this work.

Acknowledgment. The authors wish to thank CONICIT of Venezuela (Project S1-95001616) for providing funding for the SGI ORIGIN 2000 and SGI O2 workstation used in this work.

References and Notes

(1) Bader, R. F. W. *Atoms in Molecules—a Quantum Theory*; Clarendon Press: Oxford, 1990.
(2) Bader, R. F. W. *J. Phys. Chem.* **1998**, *102*, 7314.
(3) Bader, R. F. W.; Popelier, P. L. A.; Keith, T. A. *Angew. Chem., Intl. Ed. Eng.* **1994**, *33*, 620.
(4) Wiberg, K. B.; Bader, R. F. W.; Lau, C. D. H. *J. Am. Chem. Soc.* **1987**, *109*, 985.
(5) Zou, P.; Bader, R. F. W. *Acta Crystallogr.* **1994**, *A50*, 714.
(6) Eberhart, M. E. *Can. J. Chem.* **1996**, *74*, 1229.
(7) Eberhart, M. E. *Philos. Mag. A.* **1996**, *73*, 47.
(8) Eberhart, M. E.; Clougherty, D. P.; MacLaren, J. M. *J. Am. Chem. Soc.* **1993**, *115*, 5762.
(9) Eberhart, M. E.; Clougherty, D. P.; MacLaren, J. M. *J. Mater. Res.* **1993**, *8*, 438.
(10) Eberhart, M. E.; Clougherty, D. P.; MacLaren, J. M. *Philos. Mag. B.* **1993**, *68*, 455.
(11) Aray, Y.; Bader, R. F. W. *Surface Sci.* **1996**, *351*, 233.
(12) Mei, C.; Edgecombe, K.; Smith, V.; Heilingerbrunner, A. *Int. J. Quantum Chem.* **1993**, *48*, 287.
(13) Pendás, M. A.; Costales, A.; Luaña, V. *Phys. Rev. B* **1997**, *55*, 4275.
(14) Luaña, V.; Pendás, M. A.; Costales, A. *Phys. Rev. B* **1997**, *55*, 4285.
(15) Gibbs, G. V.; Hill, F. C.; Boisen, M. B. *Phys. Chem. Miner.* **1997**, *24*, 167.
(16) Gatti, C.; Saunders, V. R.; Roetti, C. *J. Chem. Phys.* **1994**, *101*, 10 686.
(17) Cargnoni, F.; Gatti, C.; Colombo, L. *Phys. Rev. B.* **1998**, *57*, 170.
(18) Blaha, P.; Schwarz, K.; Luitz, J. *WIEN 97*; Vienna University of Technology: Vienna, 1997. (Improved and updated Unix version of the original copyrighted WIEN-code, which was published by Blaha, P.; Schwarz, K.; Sorantin, P.; Trickey, S. B. *Compt. Phys. Commun.* **1990**, *59*, 399).
(19) Perdew, J. P.; Burke, S.; Ernzerhof, M. *Phys. Rev. Lett.* **1996**, *77*, 3865.
(20) Bader, R. F. W.; Krugg, P. Department of Chemistry. McMaster University, Hamilton. Ontario. Canada. 1990. (Personal communication.)
(21) Aray, Y.; Rodriguez, J.; López-Boada, R. *J. Phys. Chem.* **1997**, *101*, 2178.
(22) Barret, C. S.; Massalski, T. B. *Structure of Metals*, McGraw−Hill: USA. 1966.
(23) Hahn, T. *International Tables for Crystallography*; Kluwer Academic Publishers: Boston, 1996.
(24) Bader, R. F. W.; Essen, H. *J. Chem. Phys.* **1984**, *80*, 1943.
(25) Grimme, S. *J. Am. Chem. Soc.* **1996**, *118*, 1529.
(26) Boyd, R. J.; Choi, S. C. *Chem. Phys. Lett.* **1985**, *120*, 80.
(27) Knop, O.; Boyd, R. J.; Choi, S. C. *J. Am. Chem. Soc.* **1988**, *110*, 7299.
(28) Kittel, C. *Introduction to Solid State Physics*; John Wiley & Sons: New York, 1956.
(29) Gscheneider, K. A. *Solid State Phys.* **1964**, *16*, 275.